A Lattice Boltzmann Simulation of Mass Transport Through Composite Membranes

Li-Zhi Zhang

Key Laboratory of Enhanced Heat Transfer and Energy Conservation of Education Ministry, School of Chemistry and Chemical Engineering, South China University of Technology, Guangzhou 510640, China

DOI 10.1002/aic.14564

Published online July 30, 2014 in Wiley Online Library (wileyonlinelibrary.com)

Composite membranes with a porous support layer and a dense skin layer have been extensively used in gas separation processes. A new approach, a mesoscale Lattice Boltzmann Simulation approach, is proposed and used to model the pore-scale gas flow and mass transfer in the inhomogeneous membrane matrixes studied. Only physical forces are considered. Chemical forces are equivalently converted to physical forces through the relaxation time. Selective permeation of moisture through a composite membrane is modeled. The overall permeability is evaluated. It is found that mass transfer inhomogeneity exists not only in the porous media but also in the seemingly uniform dense skin layer. Increasing the diffusivity in the skin layer is more effective than decreasing the skin layer thickness in optimizing the overall membrane performance. The new approach gives more detailed insights into the directions for future design of composite membranes for gas separations like air dehumidification. © 2014 American Institute of Chemical Engineers *AIChE J*, 60: 3925–3938, 2014

Keywords: composite membrane, porous support layer, dense skin layer, lattice Boltzmann simulation, gas separation, mass transfer, mesoscale analysis

Introduction

Gas separation represents a major task in energy and chemical engineering. Such processes like H_2/CO_2 separation, N_2/O_2 separation, air dehumidification/humidification, gas diffusion layer, and so forth, have tremendous applications in energy and chemical production processes. Among the various technologies, composite membranes are widely used to fulfill these objectives.[1–5] The benefits with these membranes are that they combine high permeability with high selectivity. The structure of a typical composite membrane is shown in Figure 1. As seen, it is composed of two layers, one thick support layer and one thin skin layer. The support layer, usually about 100 μm in thickness, is highly porous, which only provides mechanical strength for the skin layer. An amplified view of this part is shown in Figure 1b. The skin layer, always several microns in thickness, is dense and functionalized, which provides the selectivity for the membrane. The desired gas, for instance the moisture in air, is permitted to diffuse through the skin layer. Other unwanted gases, like air, are prohibited from diffusion through the skin layer. In this way, two gases are separated apart. Since the skin layer is very thin, and the resistance in the support layer is low, permeability of the whole membrane is rather high. As a result, these membranes are very promising in gas separation operations, especially under low operating pressures which only require minimum energy costs.

Mass transfer in membranes is the key factor influencing system performance. Modeling of mass transfer in membranes has long been the focus of study. Generally, membranes are around 100 μm in thickness and their structures are highly inhomogeneous. Due to this mesoscale nature (μm) in dimensions and the difficulties in treating these inhomogeneous structures, previous modeling of membrane systems was limited to macroscale. A literature review found that in the past 20 years, relevant studies can be classified into following four categories:

1. Single layer lumped parameter model. This approach, a black box model in nature, was used in most previous simulations of membrane systems.[6–9] According to this method, mass diffusion in membranes is evaluated by an empirical lumped parameter effective diffusivity. Empirical models were summarized to relate the effective diffusivity with structural parameters. For porous membranes, Fick's model, Dusty-gas model, and the Stefan–Maxwell model[8]were used to describe the transport processes inside. For dense membranes, solution-diffusion model[10]was used to analyze the mass diffusion inside. The method is simple and easy to solve, however, the differences in membrane structures are neglected. Detailed transport phenomena inside the membrane matrixes are unknown.

2. Two-layer lumped parameter model. This is a step forward. For composite membrane, the whole membrane is divided into two layers, one porous support layer, and one dense skin layer. They are cascaded in an analogy to electric circuits in series. [2,11,12] The overall resistance is calculated by summing the resistance of two layers. With this approach,

Correspondence concerning this article should be addressed to L.-Z. Zhang at lzzhang@scut.edu.cn.

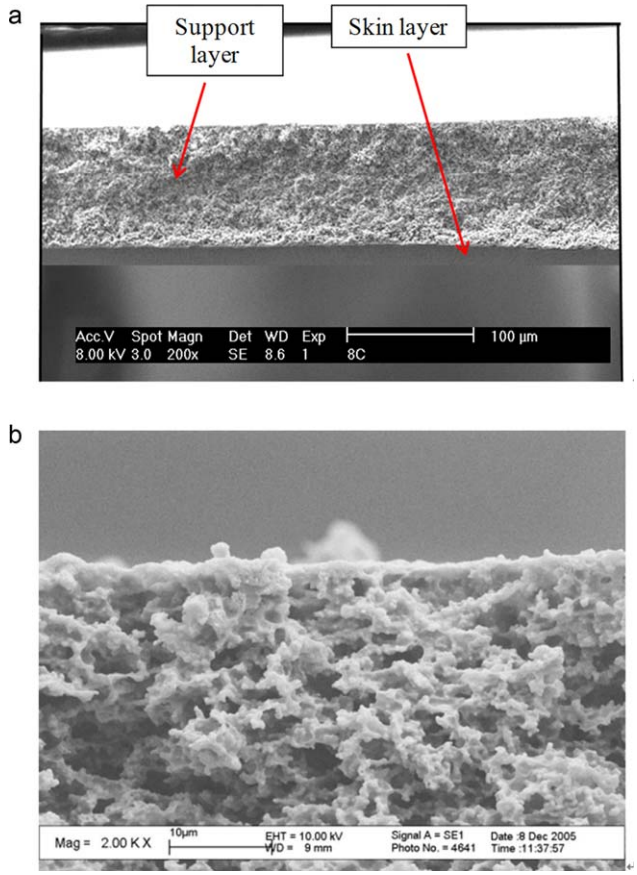

Figure 1. SEM (Scanning Electron Micrograph) of the cross sections of a composite membrane with a porous support layer and a dense skin layer.

(a) whole membrane; (b) an amplified section in the porous layer. [Color figure can be viewed in the online issue, which is available at wileyonlinelibrary.com.]

Zhang et al.[13]clarified the roles of the porous layer and the skin layer in membrane air dehumidification. This method is in fact a series of two black boxes, so it can be called a two black-box model.

3. Macroscopic CFD modeling. In studies of porous media, N-S equations in the matrix are solved to give the fluid flow and mass transfer profiles inside the structure. This volume-averaged approach is usually used to obtain macroscopic properties such as permeability (through Darcy's law), and effective diffusivity. Studied porous structures include packed beds,[14,15] sands, and soils.[16] Although popular in common porous media, this approach has seldom been used in membranes. The reason is that compared to common porous media, the membrane thickness is very small (10–100 µm). Though in-plane dimensions are similar to common porous media, their through-plane dimension is in mesoscale, which makes the use of macroscale governing N-S equations not appropriate.

4. Molecular Dynamics Simulation (MDS). This is a microscale approach. Recently, MDS has been employed to simulate the gas diffusion in porous media. The transport in a nanoporous media was modeled by Monte Carlo simulations.[17] Nonequilibrium MDSs were used to investigate the transport properties of pressure-driven water flow passing through carbon nanotube membranes.[18] Although this approach can disclose very detailed mechanisms in the microstructures, the limitation is that the calculation load is tremendously heavy even for a small fraction of membrane. Therefore, only very simple homogeneous structures can be approximated.

In a summary, for the transport phenomenon in the mesoscale membrane structure, appropriate modeling of mass transfer is still a challenging task. The mesoscale transport phenomenon requires a mesoscale approach that can reflects the complex structures in the material.

Lattice Boltzmann simulation (LBM) is just such a mesoscale modeling approach. From this respect, it provides a promising alternative. In recent years, LBM has been successfully used in modeling the mesoscale fluid flow and heat and mass transfer in porous media.[19] As for membranes, Chen et al.[20,21] modeled the fluid flow and mass diffusion in fuel cell ion exchange membranes. Similar works were also conducted by Kim and Pitsch.[22] Further, Yablecki et al.[23] studied the heat transfer in fuel cell diffusion layers with LBM. These studies are very instructive. However, in all these studies, the membranes are only approximated by simple homogeneous structures. This is not valid with the widely used high-performance composite membranes. Inhomogeneity in these structures has made the modeling difficult.

Under this background, in this study, LBM is extended to modeling of mass transfer in more complex composite membranes. The composite membrane is first reconstructed into two layers, one porous layer and one dense layer. Then, the fluid flow and mass transfer in the two structures are modeled. Consequent permeability and equivalent diffusivity are evaluated. The methodology can disclose some insight information that is unimaginable by other microscopic approaches. The approach is feasible because this mesoscale problem just requires a mesoscale modeling approach.

Reconstruction of the Membrane Structure

Figure 2 shows a schematic of the cross section of the composite membrane. It is composed of two layers: the first layer is a sponge like porous support layer and the second layer is a denser skin layer. A representing periodic section in the whole cross section is selected as the calculation domain, as surrounded by the dashed lines OABC.

Air dehumidification through vapor-permeable membranes is modeled. Modified PVDF-PVA composite membranes[13] are selected to fulfill this objective. For such thin membranes, heat released at the feed side can be balanced by the heat absorbed at the permeate side,[24] so only isothermal permeation processes are considered. Since the skin layer blocks the transport of air, only water vapor can diffuse in the membrane. The first layer, OADE in Figure 2, is an inhomogeneous porous media. The second layer, EDBC, can be regarded as a homogeneous solid part, where there are no macro gas flows. Only vapor diffuses through it.

The microstructure of the porous part depends on the manufacturing process. As observed in Figure 1, the porous part can be regarded as composing of pores and solid spheres. The density and the diameter of spheres, by a random distribution, result in different membrane structures. In this investigation, the cross sectional images of the porous part are used to reconstruct the porous media for LBM simulations. The reconstruction is performed by arranging spheres in such a way that the solid particles follow the stochastic distribution in membranes. The reconstruction procedure can be

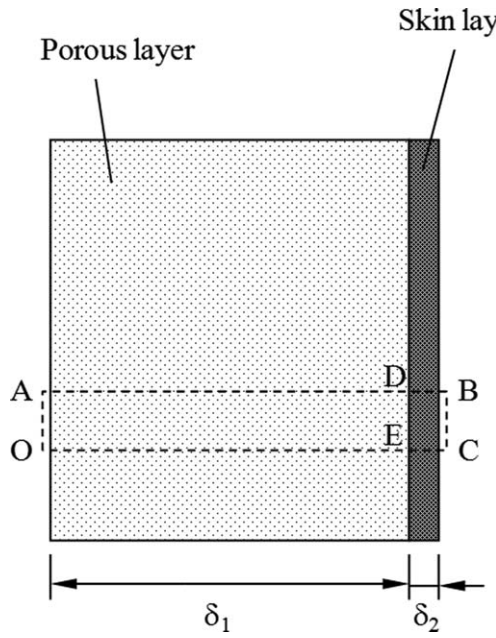

Figure 2. Schematic of the composite membrane structure.

The area surrounded by the dashed lines, OABC, is the calculating domain.

computationally realized by a modified simulated annealing method.[25,26] According to this method, a sphere is adopted as the unit element. Spheres in a computational domain randomly move to find a structure that satisfies specified statistical functions representing the solid phase distributions. This is called the Sphere-based simulated annealing method. The porous media, the first layer of membrane in this case, is considered to be of two phases, for example, the solid phase, and the voids. The two-phase porous media can be described by the index function

$$I_s(x,y)=\begin{cases}1 & (x,y) \text{ is in solid}\\ 0 & \text{otherwise}\end{cases} \tag{1}$$

Because the microstructure of porous media is complex and random, statistical moments of the index function can be used to describe the medium. The average of I_s is the volume fraction of the solid part. Then the porosity

$$\varepsilon=1.0-\langle I_s(x,y)\rangle \tag{2}$$

where angular brackets represent an ensemble average. Correlation functions are used to describe the distribution of a porous media. It is found that a combination of linear-path and two-point correlation functions is able to reflect both the intercluster and intracluster information.[25]

For statistically homogeneous media, the linear-path function, $S_{1,ij}$, is defined as the probability of finding a line segment spanning from (x,y) to distance r that lines entirely in the solid phase. The linear function is

$$S_{1,ij}(r)=\begin{cases}(L_1-r)/N & \text{when } 0\le r\le L_1\\ 0 & \text{otherwise}\end{cases} \tag{3}$$

where $N=\sqrt{N_xN_y}$, and N_x and N_y are the system size pixels in horizontal and vertical directions. L_1 is a linear cluster length, which is selected as 5 times the spheres diameter d_c.

The two-point correlation function is

$$S_{2,ij}(r)=\langle I_s(x,y)I_s((x,y)+r)\rangle \tag{4}$$

In the sphere-based simulated annealing method, porous media is represented by a collection of spheres. To generate the structure, initially, spheres are randomly allocated in a periodic box with dimensions $N_x \times N_y$. The radius of the spheres is assumed to be uniform. The contact between different spheres are permitted, however, the overlapping is not permitted. The allocation of spheres are completed when a specified volume fraction are occupied. After initialization, the spheres are randomly moved in the periodic box to realize minimum energy. The displacement during random movements can be chosen arbitrary.

After a random movement, the energy difference $\Delta E = E'\text{-}E$ between the two successive states is calculated, where the energy or error function is defined by

$$E=\sum_{k=1,2}a_k\sum_{r,i,j}\lfloor S_{k,ij}(r)-S_{k,ij,0}(r)\rfloor^2 \tag{5}$$

where the subscript "0" means the previous step, and a_k is the weight for the linear or two-point functions, $r=0\sim5d_c$, $i=1\sim N_x$, $j=1\sim N_y$.

This change of state is accepted with the probability $P(\Delta E)$[22]

$$P(\Delta E)=\begin{cases}1 & \Delta E\le 0\\ \exp(-\Delta E/T) & \Delta E>0\end{cases} \tag{6}$$

where T is a solution parameter that plays the role of temperature in the annealing system. The rate of change for T is chosen such that a system converges to the minimum energy (error) as quickly as possible, without being trapped in a local minimum state. It is suggested that the initial temperature T_0 is chosen to give an initial acceptance rate of 0.5. Then the temperature cools down at a rate of

$$T^{(n+1)}=\lambda_1 T^{(n)} \tag{7}$$

where ratio $\lambda_1=0.9$, and n is iteration step. The iterations are repeated until the error is less than a tolerance of 10^{-9}. The implementation of Eq. 6 can be realized in this manner: the movement is accepted if $[P(\Delta E)>\text{random }(0,1)]$.

The above proposed method is used to generate the porous computational domain OADE. After that, a homogeneous zone (the second layer) is added to the domain. The complete domain OABC is thus generated. Figure 3 shows a reconstructed membrane (the calculation domain OABC). In the figure for the porous part, the diameter of spheres are 5 pixels, and the porosity is 0.50. The equivalent mean pore diameter is 3.95 μm for layer 1.

The LBM Model

Fluid flow and mass transfer in the porous layer

For porous media, both air and moisture can flow freely in the pores, if without the blocking effect from the skin layer. Further, the porous part is assumed hydrophobic, so chemical reactions between the gases and the matrix are neglected. The mass transfer problem is a binary miscible fluid mixture under the condition that the fraction of the diffusing component, C_v, is negligibly small. Generally, humidity in air is less than 0.02 kg moisture/kg dry air.

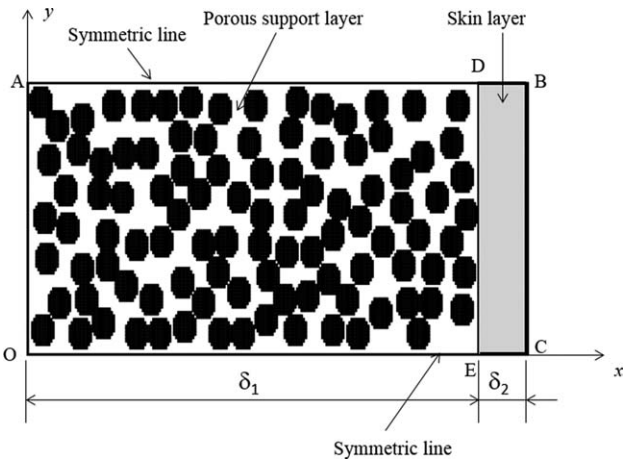

Figure 3. The reconstructed calculating domain for composite membranes.

It includes two layers: the porous support layer OADE, and the skin layer EDBC. Zone OABC corresponds to the dashed area in Figure 2.

Besides, as mentioned, only isothermal mass transfer is considered. Further, the range of applicability: only physical forces are considered. Chemical forces in the skin layer are equivalently converted to physical forces by the equivalent diffusivity.

The two dimensional nine-velocity (D2Q9) model[27] is used in the following calculations, where the physical space is divided into rectangular lattices. Hereafter, nondimensional variables, which are defined by a characteristic length x_0, a characteristic particle speed c_0, a characteristic time scale t_0 ($c_0 = x_0/t_0$), a reference density ρ_0, and a reference mass uptake C_0 (kg vapor/kg dry air) are used. All the parameters are normalized by these characteristic parameters. In the following, all the variables are dimensionless and in lattice scales, unless donated by a superscript "′," and/or mentioned with physical dimensions. The nine-velocity model has the following dimensionless velocity vectors as shown in Figure 4

$$[\mathbf{e}_0,\mathbf{e}_1,\mathbf{e}_2,\mathbf{e}_3,\mathbf{e}_4,\mathbf{e}_5,\mathbf{e}_6,\mathbf{e}_7,\mathbf{e}_8] = \begin{bmatrix} 0 & 1 & 0 & -1 & 0 & 1 & -1 & -1 & 1 \\ 0 & 0 & 1 & 0 & -1 & 1 & 1 & -1 & -1 \end{bmatrix} \quad (8)$$

The evolutions of the particle distribution functions, $f_i(\mathbf{x},t)$ for the fluid (air and vapor gas mixture) and $g_i(\mathbf{x},t)$ for the diffused species (vapor), with velocity at the point $\boldsymbol{x}$ and time t are computed by the following BGK collision and streaming equations[27–29]

$$f_i(\mathbf{x}+\mathbf{e_i}\Delta t, t+\Delta t) - f_i(\mathbf{x},t) = -\frac{\Delta t}{\tau_v}\left[f_i(\mathbf{x},t) - f_i^{eq}(\mathbf{x},t)\right] \quad (9)$$

$$g_i(\mathbf{x}+\mathbf{e_i}\Delta t, t+\Delta t) - g_i(\mathbf{x},t) = -\frac{\Delta t}{\tau_m}\left[g_i(\mathbf{x},t) - g_i^{eq}(\mathbf{x},t)\right] \quad (10)$$

for $i = 0, 1, 2, \ldots, 8$, where Δt is time step; f_i^{eq}, and g_i^{eq} are equilibrium distribution functions; τ_v and τ_m are relaxation times. The equilibrium distribution functions are defined by[19] and modified to account for the concentration unit of C_v (kg vapor/kg dry air, if with dimensions)

$$f_i^{eq}(\mathbf{x},t) = \rho W_i\left[1 + \frac{e_i\cdot\boldsymbol{u}}{c_s^2} + \frac{(e_i\cdot\boldsymbol{u})^2}{2c_s^4} - \frac{\boldsymbol{u}^2}{2c_s^2}\right] \quad (11)$$

$$g_i^{eq}(\mathbf{x},t) = \rho C_v W_i\left[1 + \frac{e_i\cdot\boldsymbol{u}}{c_s^2}\right] \quad (12)$$

where W_i are the weight coefficients, bold variables (like $\boldsymbol{u}$, $\boldsymbol{x}$, $\boldsymbol{J}$, etc) mean vectors, and c_s is the lattice sound speed given by

$$c_s = \frac{c}{\sqrt{3}} \quad (13)$$

$$c = \frac{\Delta x}{\Delta t} \quad (14)$$

where c is lattice speed, and Δx is lattice spacing. In this lattice structure, the spacings in x, y, and time t are all selected as 1.0, so the lattice speed is 1.0. For the current D2Q9 lattice structure, the weight coefficients are: $W_0 = 4/9$; $W_{1-4} = 1/9$; $W_{5-8} = 1/36$.[19,27]

The density and velocity of the fluid are given by

$$\rho = \sum_i f_i \quad (15)$$

$$\rho\boldsymbol{u} = \sum_i \mathbf{e}_i f_i \quad (16)$$

The concentration and mass flux of vapor are given by

$$\rho C_v = \sum_i g_i \quad (17)$$

$$\mathbf{J}_v = \sum_i \mathbf{e}_i g_i \quad (18)$$

The relaxation time for fluid flow is related to kinematic viscosity by

$$\tau_v = \frac{v}{c_s^2\Delta t} + 0.5 \quad (19)$$

An expression is given for the relaxation time for mass diffusion.[19] However, it is found in the current study that it would lead to unrealistic concentration distributions. So a new expression in a form similar to Eq. 19 is proposed for mass relaxation time. It is[19]

$$\tau_m = \frac{D_v}{c_s^2\Delta t} + 0.5 \quad (20)$$

Pressure of the fluid

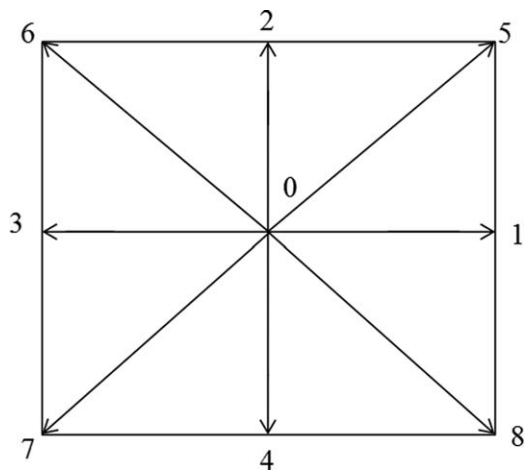

Figure 4. Velocity vectors in a D2Q9 lattice model.

$$p=\rho c_s^2 \tag{21}$$

Mass Diffusion in the Skin Layer. Only moisture can transfer in the skin layer. Solution-diffusion is the mechanism for gas transfer in the dense solid membranes. According to this mechanism, moisture diffuses in an "adsorbed phase," or "water phase,"which is in equilibrium with gas phase by the following equation

$$C_w=K_p C_v \tag{22}$$

where C_w is uptake of water in membrane (kg water/kg membrane), K_p is partition coefficient.

Moisture diffusion is governed by

$$J_v=\rho_m D_{wm}\frac{\partial C_w}{\partial x}=\rho_m K_p D_{wm}\frac{\partial C_v}{\partial x}=\rho_a D_{e2}\frac{\partial C_v}{\partial x} \tag{23}$$

$$D_{e2}=\frac{\rho_m K_p D_{wm}}{\rho_a} \tag{24}$$

where D_{wm} is water diffusivity in membrane (the second layer), D_{e2} is the equivalent vapor diffusivity in the membrane (the second layer). ρ_a is air density in the hypothetic space of layer two, which can be selected as the constant ρ_0.

From Eq. 23, water diffusion in this layer can be regarded as an equivalent vapor diffusion with diffusivity D_{e2}. So the LBM model proposed in above sections for the first layer can also be used to predict moisture diffusion in the second layer, if D_v is replaced by D_{e2}. Then

$$\tau_{m2}=\frac{D_{e2}}{c_s^2\Delta t}+0.5 \tag{25}$$

At this step, the water diffusion is converted to equivalent vapor diffusion in this homogeneous "void" space.

Boundary conditions

In LBM simulations, distribution functions rather than macro variables are required on the boundaries of the calculating domain. For the composite membrane with skin layer, there will be no macro flows in the matrix. In this case, only mass boundary conditions are required. However, for a more general purpose, and also for model validations, boundary conditions for both flow and mass transfer are provided here.

Fluid flow in porous media

If the skin layer in Figure 3 is removed, and the membrane is operated under pressure (density) differences, there will be macro flows inside. At the inlet face OA in Figure 3, where the inlet density is known, the boundary conditions proposed by Zou and He[30] is used, which are based on an idea of bounce back of nonequilibrium part of the distribution. According to this concept, for the inlet face OA, the macro variables of the boundary conditions are: $\rho=\rho_{in}$, $u_y=0$. At the inlet face after streaming, f_1, f_5, f_8 are unknown, and other functions are known. Then based on mass and momentum balance equations of Eqs. 15 and 16, macro velocity in x axis is calculated by

$$u_x=1-\frac{f_0+f_2+f_4+2(f_3+f_6+f_7)}{\rho_{in}} \tag{26}$$

By bounce-back the nonequilibrium part of f_3 ($f_3-f_3^{eq}=f_1-f_1^{eq}$), f_1 is expressed as[30]

$$f_1=f_3+\frac{2}{3}\rho_{in}u_x \tag{27}$$

Then other two functions can be obtained by momentum balance

$$f_5=f_7-\frac{1}{2}(f_2-f_4)+\frac{1}{6}\rho_{in}u_x \tag{28}$$

$$f_8=f_6+\frac{1}{2}(f_2-f_4)+\frac{1}{6}\rho_{in}u_x \tag{29}$$

For the upper corner point on the inlet face (point A), f_1, f_4, f_5, f_7, f_8 are unknown. The boundary conditions at the upper surface AB are symmetric, so at point A, $f_4=f_2$, $f_7=f_6$. Other functions can be calculated by Eqs. 26–29.

Similarly, for the lower corner on the inlet face (point O), f_1, f_2, f_5, f_6, f_8 are unknown. The boundary conditions at the lower surface OC are symmetric, so at the lower corner of the inlet face, $f_2=f_4$, $f_6=f_7$. Other functions can also be calculated by Eqs. 26–29.

At the outlet boundary of ED in Figure 3, fully developed boundary conditions are assumed. Then, the distribution functions are set to those of the neighboring interior nodes

$$f_j^{(Nx)}=f_j^{(Nx-1)} \tag{30}$$

where N_x is the nodes at the outlet face, and N_x-1 is the neighboring interior nodes.

As have mentioned, the upper wall AB is a symmetric boundary, then on this surface, the unknown functions are calculated by $f_4=f_2$, $f_7=f_6$, $f_8=f_5$. Similarly, at the lower surface OC, the three unknown functions are calculated by $f_2=f_4$, $f_6=f_7$, $f_5=f_8$.

Interior solid cells

On the surfaces of the solid cells in the porous media, bounce-back scheme is used to achieve the nonslip boundary conditions. To alleviate the influences of inlet and outlet flow, additional 30 nodes are added before and after the membrane domain. Inlet and outlet boundaries are exerted on the extended inlet and outlet surfaces.

Mass transfer boundary conditions

At the inlet and outlet, constant mass fractions are assumed. The distribution functions are evaluated from macroscopic concentrations. The operators that reconstruct the distribution functions in the LBM from macro parameters are required. The distribution functions are described up to the first-order nonequilibrium terms.

Here, we have developed an algorithm to transfer the macro concentrations into concentration distribution functions with a scheme similar to[29]

$$g_i=g_i^{eq}+g_i^{(1)} \tag{31}$$

The Chapman–Enskog expansion is applied to the lattice Boltzmann equation, then the first order of nonequilibrium is described by

$$\begin{aligned} g_i^{(1)}=-\tau_m\Delta t\cdot\Bigg[&U_{ix}\frac{g_i^{eq}}{\rho C_v}\frac{\partial(\rho C_v)}{\partial x}+U_{iy}\frac{g_i^{eq}}{\rho C_v}\frac{\partial(\rho C_v)}{\partial y}\\ &+\frac{W_i\rho C_v U_{ix}e_{iy}}{c_s^2}\frac{\partial u_y}{\partial x}+\frac{W_i\rho C_v U_{iy}e_{ix}}{c_s^2}\frac{\partial u_x}{\partial y}-g_i^{eq}\frac{\partial u_x}{\partial x}\\ &-g_i^{eq}\frac{\partial u_y}{\partial y}-W_i C_v e_{ix}\frac{\partial\rho}{\partial x}-W_i C_v e_{iy}\frac{\partial\rho}{\partial y}\Bigg] \end{aligned} \tag{32}$$

where

$$U_{i\alpha}=e_{i\alpha}-u_\alpha \tag{33}$$

and here $\alpha = x, y$.

The detailed procedure for deduction of the first-order nonequilibrium part of distribution function can be found in Appendix A.

First and second layer interface

At the interface between the first layer and the second layer, DE in Figure 3, conjugate mass transfer boundary condition is exerted. That means at the interface, the mass fraction (mass continuity) and the mass flux (flux continuity) in layer one equal to those in layer two, respectively, or, $C_{v1} = C_{v2}$; and $\boldsymbol{J}_{v1} = \boldsymbol{J}_{v2}$. For layer one, at the interface DE, g_3, g_6, and g_7 are unknown. For layer two, at the interface DE, g_1, g_5, and g_8 are unknown. From Eq. 17, following conservation forms are obtained

$$g_3^{\mathrm{p}}+g_6^{\mathrm{p}}+g_7^{\mathrm{p}}=\rho^{\mathrm{p}}C_{v1}-g_0^{\mathrm{p}}-g_1^{\mathrm{p}}-g_2^{\mathrm{p}}-g_4^{\mathrm{p}}-g_5^{\mathrm{p}}-g_8^{\mathrm{p}} \tag{34}$$

$$g_1^{\mathrm{s}}+g_5^{\mathrm{s}}+g_8^{\mathrm{s}}=\rho^{\mathrm{s}}C_{v2}-g_0^{\mathrm{s}}-g_2^{\mathrm{s}}-g_3^{\mathrm{s}}-g_4^{\mathrm{s}}-g_6^{\mathrm{s}}-g_7^{\mathrm{s}} \tag{35}$$

where superscript "p" and "s" refer to first layer (porous) and second layer (skin) side, respectively. For the interface in the composite membrane, macro velocity $u_x = 0$, therefore, based on Eq. 18, following conservation forms can be obtained

$$J_{v1}=g_1^{\mathrm{p}}+g_5^{\mathrm{p}}+g_8^{\mathrm{p}}-g_3^{\mathrm{p}}-g_6^{\mathrm{p}}-g_7^{\mathrm{p}} \tag{36}$$

$$J_{v2}=g_1^{\mathrm{s}}+g_5^{\mathrm{s}}+g_8^{\mathrm{s}}-g_3^{\mathrm{s}}-g_6^{\mathrm{s}}-g_7^{\mathrm{s}} \tag{37}$$

Adopting a technique similar to,[19] two sums of the unknown functions, g_r^{p} and g_r^{s}, are introduced. It is assumed that the unknown functions are allocated based on their weights, or

$$\begin{aligned} &g_3^{\mathrm{p}}=W_3 g_r^{\mathrm{p}},\ g_6^{\mathrm{p}}=W_6 g_r^{\mathrm{p}},\ g_7^{\mathrm{p}}=W_7 g_r^{\mathrm{p}},\ \text{and}\ g_1^{\mathrm{p}}=W_1 g_r^{\mathrm{p}},\\ &g_5^{\mathrm{p}}=W_5 g_r^{\mathrm{p}},\ g_8^{\mathrm{p}}=W_8 g_r^{\mathrm{p}} \end{aligned} \tag{38}$$

then it has

$$g_3^{\mathrm{p}}+g_6^{\mathrm{p}}+g_7^{\mathrm{p}}=(W_3+W_6+W_7)g_r^{\mathrm{p}} \tag{39}$$

$$g_1^{\mathrm{s}}+g_5^{\mathrm{s}}+g_8^{\mathrm{s}}=(W_1+W_5+W_8)g_r^{\mathrm{s}} \tag{40}$$

Considering $C_{v1} = C_{v2}$, subtracting Eq. 34 by 35, and then substituted by Eqs. 39 and 40 gives

$$\begin{aligned} &\frac{(W_3+W_6+W_7)}{\rho^{\mathrm{p}}}g_{\mathrm{r}}^{\mathrm{p}}-\frac{(W_1+W_5+W_8)}{\rho^{\mathrm{s}}}\\ &g_{\mathrm{r}}^{\mathrm{s}}=-\frac{\left(g_0^{\mathrm{p}}+g_1^{\mathrm{p}}+g_2^{\mathrm{p}}+g_4^{\mathrm{p}}+g_5^{\mathrm{p}}+g_8^{\mathrm{p}}\right)}{\rho^{\mathrm{p}}}\\ &+\frac{\left(g_0^{\mathrm{s}}+g_2^{\mathrm{s}}+g_3^{\mathrm{s}}+g_4^{\mathrm{s}}+g_6^{\mathrm{s}}+g_7^{\mathrm{s}}\right)}{\rho^{\mathrm{s}}} \end{aligned} \tag{41}$$

Considering $J_{v1} = J_{v2}$, subtracting Eq. 36 by 37, and then substituted by Eqs. 39 and 40 gives

$$(W_3+W_6+W_7)g_{\mathrm{r}}^{\mathrm{p}}+(W_1+W_5+W_8)g_{\mathrm{r}}^{\mathrm{s}}=g_1^{\mathrm{p}}+g_5^{\mathrm{p}}+g_8^{\mathrm{p}}+g_3^{\mathrm{s}}+g_6^{\mathrm{s}}+g_7^{\mathrm{s}} \tag{42}$$

Solution of Eqs. 41 and 42 will have the following equations for g_r^{p} and g_r^{s}

$$g_r^{\mathrm{p}}=\frac{c_1}{(\rho^{\mathrm{p}}+\rho^{\mathrm{s}})(W_3+W_6+W_7)} \tag{43}$$

$$\begin{aligned} c_1=&-\rho^{\mathrm{s}}\left(g_0^{\mathrm{p}}+g_1^{\mathrm{p}}+g_2^{\mathrm{p}}+g_4^{\mathrm{p}}+g_5^{\mathrm{p}}+g_8^{\mathrm{p}}\right)\\ &+\rho^{\mathrm{p}}\left[g_0^{\mathrm{s}}+g_2^{\mathrm{s}}+g_4^{\mathrm{s}}+2\left(g_3^{\mathrm{s}}+g_6^{\mathrm{s}}+g_7^{\mathrm{s}}\right)+g_1^{\mathrm{p}}+g_5^{\mathrm{p}}+g_8^{\mathrm{p}}\right] \end{aligned} \tag{44}$$

$$g_r^{\mathrm{s}}=\frac{c_2}{(\rho^{\mathrm{p}}+\rho^{\mathrm{s}})(W_1+W_5+W_8)} \tag{45}$$

$$\begin{aligned} c_2=&-\rho^{\mathrm{p}}\left(g_0^{\mathrm{s}}+g_2^{\mathrm{s}}+g_3^{\mathrm{s}}+g_4^{\mathrm{s}}+g_6^{\mathrm{s}}+g_7^{\mathrm{s}}\right)\\ &+\rho^{\mathrm{s}}\left[g_0^{\mathrm{p}}+g_2^{\mathrm{p}}+g_4^{\mathrm{p}}+2\left(g_1^{\mathrm{p}}+g_5^{\mathrm{p}}+g_8^{\mathrm{p}}\right)+g_3^{\mathrm{s}}+g_6^{\mathrm{s}}+g_7^{\mathrm{s}}\right] \end{aligned} \tag{46}$$

At this step, the unknown functions can be calculated by Eq. 38.

Performance indices

When the mass concentration and fluxes are calculated and known, transport properties can be calculated. Permeability of the membrane is calculated by partial pressure difference

$$Pe=\frac{J_v\delta v}{\Delta(pC_v)} \tag{47}$$

where δ is membrane thickness in lattice unit; and $\Delta(pC_v)$ is the partial pressure difference across the membrane.

Effective diffusivity of the membrane

$$D_e=\frac{J_v\delta}{\Delta(\rho C_v)} \tag{48}$$

where $\Delta(\rho C_v)$ is the concentration difference across the membrane. It should be noted that this value has already considered the effects of porosity and tortuosity, two empirical parameters often encountered in membrane analysis.

For porous membranes, established theories governing the transport of gas in pores are Poiseuille flow and Knudsen diffusion. An index for which mechanism is dominant is the Knudsen number defined by

$$Kn=\frac{\lambda_v}{d_p}=\frac{Ma}{\mathrm{Re}}\sqrt{\frac{r_1\pi}{2}} \tag{49}$$

where λ_v is the mean free path of the diffused gas, and d_p is pore diameter in membranes; r_1 is specific heat ratio of diffused gas, which is 1.4 for air and 1.34 for vapor. Ma ($= u_m/c_s$) and Re ($= u_m d_p/v$) are Mach and Reynolds numbers, respectively.

When $Kn < 0.01$, Poiseuille viscous flow is dominant. The Bulk velocity through a pore is[31]

$$u_m=\frac{d_p^2\Delta p_v}{32\rho C_v v\delta} \tag{50}$$

Considering equivalent diffusion equation

$$J_v=\rho u_m C_v=D_p\frac{\Delta(\rho C_v)}{\delta} \tag{51}$$

Then the equivalent Poiseuille diffusivity is calculated by

$$D_p=\frac{d_p^2 c_s^2}{32v} \tag{52}$$

When $Kn \geq 10$, Knudsen diffusion is dominant. Knudsen diffusivity is calculated by[31]

$$D_K=\frac{d_p c_s}{3}\sqrt{\frac{8}{\pi\cdot r_1}} \tag{53}$$

Dimensional physical properties

In engineering, it is more direct to use the parameters with dimensions. The above variables are in lattice units or

dimensionless. They are converted to real physical parameters by the following relations

$$\rho' = \rho \cdot \rho_0 \tag{54}$$

$$\delta' = \delta \cdot x_0 \tag{55}$$

$$t' = t \cdot t_0 \tag{56}$$

$$u' = u \cdot \frac{x_0}{t_0} = uc_1 \tag{57}$$

$$C_v^{'} = C_v \cdot C_0 \tag{58}$$

$$J_v^{'} = J_v \cdot \rho_0 C_0 \frac{x_0}{t_0} \tag{59}$$

$$\nu' = \nu \frac{x_0^2}{t_0} \tag{60}$$

Diffusivities

$$D' = D \frac{x_0^2}{t_0} \tag{61}$$

$$D_e^{'} = D_e \frac{x_0^2}{t_0} \tag{62}$$

$$Pe^{'} = Pe \cdot x_0^2 \tag{63}$$

Solution procedure

For each simulation, grid independence test is done to ensure the final results are insensitive to grids resolution (grid dependence $< 10^{-5}$). A 226 $\times$ 80 resolution is selected for membranes. Then simulations are performed on the grids structure selected. The procedures include:

1. Membrane preparation. Porous PVDF membranes are first made and characterized as described in.[13] Their SEMs are observed to know the internal structures. Membrane parameters like porosity, thickness are measured. After the membranes are fabricated, their permeability is measured in a FLEC system built in our laboratory,[32] where the operating conditions are designed to let the Poiseuille flow dominant. Then, the effective pore diameters for the porous membranes are evaluated by the relations between pore diameters and permeability, Eqs. 50–52. This is the test data, with an accuracy $\pm 2\%$. Then, a modified PVA skin layer is coated on the porous support membrane.[13] The composite membrane is characterized. The properties like the thickness of the skin layer, partition coefficient and density are measured.

2. Porous media reconstruction and grid generation. With parameters determined in step (1), the equivalent porous media matrix for first layer is reconstructed by the simulated annealing method described in previous section. Then without a skin layer, transmembrane pressure differences are exerted on the porous membranes, and the flow fields and concentration fields are modeled. The effective pore diameters for the porous membranes are calculated. If the calculated pore diameters differ from the tested data (relative error larger than 10^{-3}), the diameters of the spherical cells used to build the porous media are revised. Step (1) is reperformed and the structures are rebuilt. The procedures stop until the predicted data agrees with the measured data.

Then numerically a homogeneous "blank" second layer is added to the first layer. The composite membrane is thus formed. Two blank buffer zones are added before and after the membrane domain to comprise the whole calculating domain. The blank buffer zones are not shown in the subsequent figures. Grids are generated on the calculation domain. By the definition of characteristic scales, the real physical units are all converted to lattice units.

3. Initialization. On the reconstructed domain, initial parameters are set: ρ, u, Cv, ν, D, and τ_v, τ_m; Time steps for velocity and concentration calculations may be different depending on the values of viscosity and diffusivity. Initial distribution functions are set as the equilibrium functions calculated by Eqs. 11 and 12.

4. Composite membrane calculation. Collision-streaming is performed across the whole domain for concentration functions calculations, with Eq. 10. Boundary conditions are incorporated to calculate the functions at boundaries and interfaces. Concentration and mass fluxes in the two layers are calculated by Eqs. 17 and 18. Then the equilibrium functions are recalculated. At last, go forward to the next time step. These steps are repeated until steady state conditions are reached with the results between two consecutive iterations are less than 10^{-7}. The calculation is second order. After fluid flow converged (with only the first layer), mass concentrations are calculated.

5. Transport data. With the calculated concentration fields, performances are calculated with Eqs. 47–53. The data are further converted back to real physical units by Eqs. 54–63.

Results and Discussion

Methodology verification

Flow and Mass Transfer in a Parallel-Plate Channel. Prior to solving the mass transfer problem in composite membranes, the numerical procedure is validated first. Flow and mass transfer in a parallel-plate channel, shown in Figure 5, is one of the most well-established benchmark for numerical validation. In the figure, AB is duct inlet, and CD is duct outlet. AC and BD are two neighboring plates, between which air flows. Duct height is H, and the consequent hydrodynamic diameter is $2H$.

In this section, the proposed LBGK procedure is applied to the flow and mass transfer in the parallel-plate channel. Two buffer zones are added to the channel ABDC before the inlet and after the outlet to form the whole domain. Rectangular grids with a resolution of 480 $\times$ 40 are generated. Surface AB is set to density inlet boundary condition, and CD is set to fully developed outlet flow boundary condition, as described in above sections. Bounce-back conditions rather than symmetric boundary conditions are exerted on plates AC and BD to realize a nonslip flow. When the pressure difference across the channel is small enough (incompressible), a Poiseuille flow is realized.

For mass transfer, constant concentration boundary conditions are set for inlet surface AB ($C_{v,in} = 1.0$) and two plates AC and BD ($C_{vw} = 0.5$). Fully developed mass transfer boundary conditions are set for the outlet face CD. As seen, this is a uniform wall mass concentration boundary condition for channel flow. The collision and streaming processes are also implemented at the grids on the wall surfaces. The method is second-order accuracy.

For channel flow, following parameters are defined:

Reynolds number

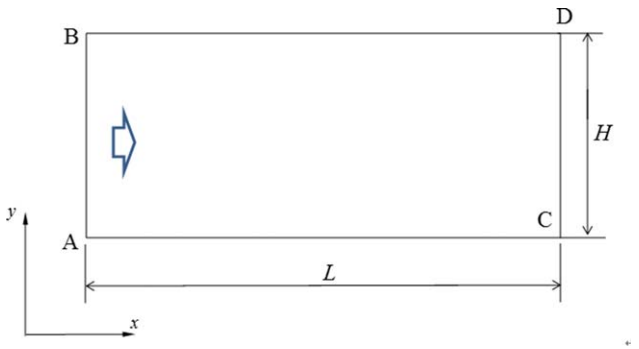

Figure 5. Flow in a parallel-plate channel.

AB, inlet face; DC, outlet face; AC and BD, duct wall surfaces. [Color figure can be viewed in the online issue, which is available at wileyonlinelibrary.com.]

$$\mathrm{Re}=\frac{2u_{\mathrm{in}}H}{v} \tag{64}$$

where u_{in} is the mean velocity at inlet. Friction factor is defined by

$$f_r=\frac{2H\frac{\Delta p}{\Delta x}}{\frac{1}{2}\rho u_{\mathrm{in}}^2} \tag{65}$$

Sherwood number

$$Sh=\frac{2kH}{D} \tag{66}$$

where k is convective mass-transfer coefficient calculated by

$$k=-\frac{D}{(\rho C_{\mathrm{v}})_{\mathrm{m}}-(\rho C_{\mathrm{v}})_{\mathrm{w}}}\frac{\partial(\rho C_{\mathrm{v}})}{\partial y}\bigg|_{y=0} \tag{67}$$

where $(\rho C_{\mathrm{v}})_{\mathrm{m}}$ is the bulk mean concentration at a duct cross section.

When Poiseuille flow is created in the parallel channel, there is analytical solution for velocity profiles. It is a parabolic expressed by[33]

$$u_{\mathrm{x}}=-\frac{\partial p}{\partial x}\frac{H^2}{2\rho v}\left(\frac{y}{H}-\frac{y^2}{H^2}\right) \tag{68}$$

Figure 6 shows the parabolic distribution of axial velocities across the channel cross section under $\Delta\rho=0.05$. Both the analytical solution and the LBM simulated values are plotted. As seen, the prediction is very satisfactory. Maximum deviations are less than 1%.

For laminar flow in duct, the product of friction and Re is a constant. The simulated ($f{\cdot}Re$) is 96.07, which is very close to the data ($f{\cdot}Re=96.0$ for parallel plates duct) provided in.[34] Therefore, fluid flow is predicted very well by the current procedure.

Mass transfer in the channel is also calculated. Calculated mass fraction contours and flux vectors are plotted in Figure 7. Operating conditions are $Re=127$. As seen, the profiles propagate along the flow with mass exchanging between the fluid and the two plates.

For fully developed laminar flow in duct under uniform mass concentration boundary conditions on walls, local Sherwood number is a constant, $Nu=Sh=7.54$.[34,35] Calculated Sherwood number in this case is 8.05, a value closer to the fully developed value. This also indicates that the flow is

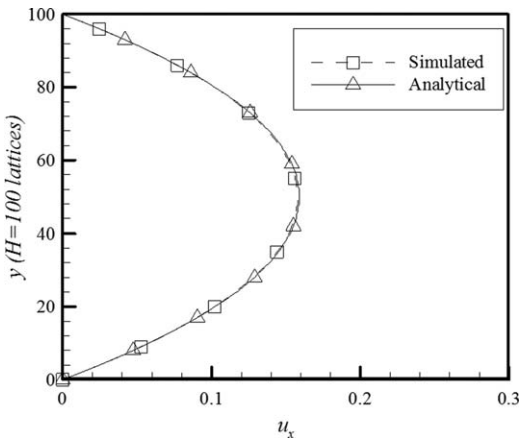

Figure 6. Transverse velocity of Poiseuille flow across the duct cross section at $\Delta\rho=0.05$, simulated and analytical solution.

nearly fully developed. As seen, both fluid flow and mass transfer are verified.

Pure Diffusion in a Rectangular Duct. Besides fluid flow and mass transfer in a parallel-plate channel, the procedure is also used to predict the effective mass diffusivity in a rectangular duct with no macro velocity. The simulated duct is similar to the channel shown in Figure 5. Fluid velocity is set to zero throughout the duct. Density throughout the duct is set to $\rho=1.0$. The inlet concentration at surface AB is set to $C_{\mathrm{v,in}}=1.0$, and outlet face CD is set to $C_{\mathrm{v,out}}=0.01$. Boundaries AC and BD are set to symmetric boundaries. Vapor diffuses in the duct with a physical diffusivity $D_{\mathrm{v}}^{'}=2.825\times10^{-5}$ m^2/s. Since there is no macro velocity in the cavity, the mass transfer is pure diffusion. For this simple object, the governing equation and its analytical solution for

$$\frac{\partial^2 C_{\mathrm{v}}}{\partial x^2}=0,\ \text{with}\ C_{\mathrm{v}}=C_{\mathrm{v,in}}\ \text{at}\ x=0;\ \text{and}\ C_{\mathrm{v}}=C_{\mathrm{v,out}}\ \text{at}\ x=L \tag{69}$$

and

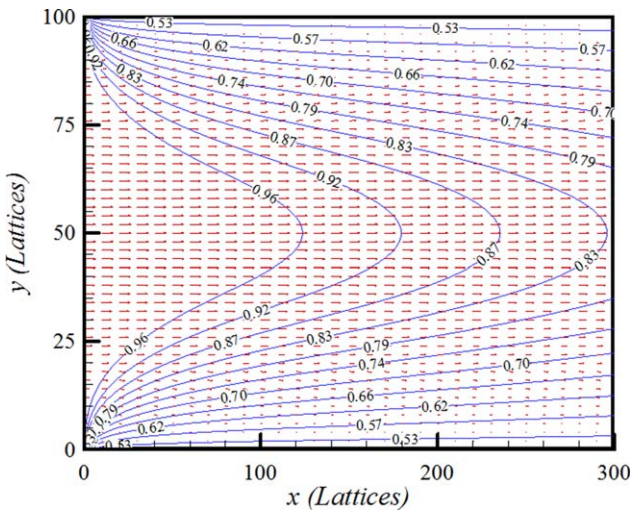

Figure 7. Mass flux vectors (red arrows), and concentration contours (blue lines) of duct flow at $Re=127$. $C_{\mathrm{v,in}}=1.0$, $C_{\mathrm{vw}}=0.5$.

[Color figure can be viewed in the online issue, which is available at wileyonlinelibrary.com.]

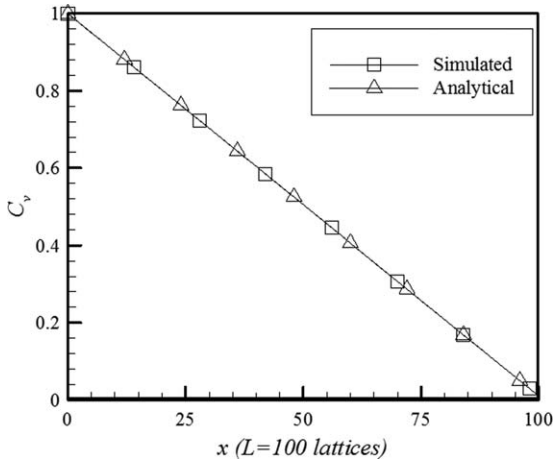

Figure 8. Comparisons of axial concentration distributions in the duct shown in Figure 5.

The macro velocities in the duct are set to 0. Other boundary conditions: AB, inlet surface; CD, outlet surface; AC and BD adiabatic surfaces (no mass flux).

$$C_v(x) = \frac{C_{v,in} - C_{v,out}}{L} x + C_{v,in} \tag{70}$$

respectively.

The LBM calculated concentration distributions and the analytically obtained concentrations are both plotted in Figure 8. As seen, the simulated matches the analytical very successfully. The profiles are exactly linearly developing from the inlet to the outlet, as governed by Eq. 70. The maximum differences between the calculated and the analytical solution are less than 10^{-5}. A further step is to evaluate the effective diffusivity calculated by LBM. The calculated effective diffusivity from Eqs. 48 and 61 is 2.817×10^{-5} m^2/s, a value very close to the diffusivity of vapor in air (2.825×10^{-5} m^2/s) that is used in the estimation of Eq. 20. At this step, the procedure is verified again.

Fluid Flow and Mass Transfer Through the Porous Layer. The porous support layer only provides mechanical support. All gases can permeate through it. If operated under pressure differences, macro fluid flows will exist. To study its mass transfer properties in this case, the skin layer is not added to the first layer first. Only the first layer is modeled.

Six porous membranes are simulated. Their structural characteristics are listed in Table 1. They are the PVDF membranes made. The porosity and thickness are characterized first. After permeability tests,[32] the mean pore diameters are deduced. These are the measured data. Then the porous media is reconstructed and LBM is performed. After the calculation of fluid flow and concentration profiles, the permeability is calculated. The mean pore diameters are then obtained. They are the calculated pore diameters. If the calculated deviates from the measured data, reconstruction is reperformed with revised spherical cell diameters. When the measured and calculated mean pore diameters are in agreement, performance is evaluated. The characteristic parameters for the simulation are: $t_0 = 1.0\times10^{-8}$ s; $x_0 = 5.0\times10^{-7}$ m; $\rho_0 = 1.2$ kg/m^3; $C_{vo} = 0.02$ kg/kg. Other properties are selected to those of moisture and air at 20°C.

Flow and concentration fields are calculated. Figure 9 shows the macro velocity vectors in MEM 5. As seen, the flow is rather inhomogeneous. Most of the fluids flow in the cavities in the membrane. Figure 10 shows the mass flux vectors inside the membrane. The pattern is very similar to that of fluid flow. Concentration contours in the matrix are plotted in Figure 11. The concentration gradients are very small in places where the solid cells are distributed sparsely, while they are steep in places where the solid cells are densely populated. Observing form these figures found that the effects of heterogeneity are obvious. The fluid flow and mass transfer are rather inhomogeneous even in such seemingly homogeneous porous membranes. However, generally, all the isolines are nearly vertical to membrane thickness, meaning nearly all mass transfer is in axial directions. Mass transfer in thickness is more prominent than that in other two dimensions. These features cannot be disclosed with common macroscopic numerical methods. The benefits with LBM are straightforward: it can disclose pore scale details inside the membranes.

The permeability and effective diffusivity are calculated with the concentration fields and are listed in Table 1. Also the measured permeability is listed. As seen, the calculated and measured permeability are in good agreement.

For different membranes, a general trend is that the higher the pore diameters and porosity are, the larger the effective diffusivity is. The resulted permeability is also higher. Based on the range of Knudsen numbers ($0.01<Kn<10$), the dominant mechanisms are neither Knudsen diffusion nor Poiseuille flow, but a combination of ordinary diffusion and Poiseuille flow. The final effective diffusivity is larger than ordinary diffusivity, as a result of macro fluid flow. From Table 1, it is also observed that the current Peclet number ($Pe = ud_p/D$) is around below 10, so both Poiseuille convection and diffusion are dominant in mass transfer. When the Peclet number is higher than 10, Poiseuille flow will be dominant and the diffusion term can be neglected. In a summary, such membranes have high permeability due to high porosity and large pore diameters.

Mass Transfer in the Composite Membrane. Now the skin layer is added to the porous layer. The whole membrane structure has been depicted in Figure 3. Because air is blocked

Table 1. Simulated Results for the Porous Membranes Under Pressure Difference

Parameters	MEM 1	MEM 2	MEM 3	MEM 4	MEM 5	MEM 6
δ_1(μm)	108.1	110.3	105.8	111.5	106.4	108.1
ε_1	0.51	0.50	0.54	0.71	0.71	0.69
d_{p1} (μm)	4.55	3.95	4.52	5.35	6.55	9.9
$\Delta p/p_0$	0.05	0.05	0.05	0.05	0.05	0.05
Kn	0.152	0.175	0.152	0.129	0.105	0.304
Peclet number	0.006	0.004	0.005	0.009	0.016	0.056
Pe, permeability (calculated, 10^{-13}m^{-2})	6.44	4.88	6.40	8.94	13.41	30.63
Pe (measured, 10^{-13}m^{-2})	6.87	5.12	7.23	9.45	12.88	32.66
D_{eff} (10^{-5} m^{2}s^{-1})	3.86	2.56	3.35	4.69	7.03	16.07

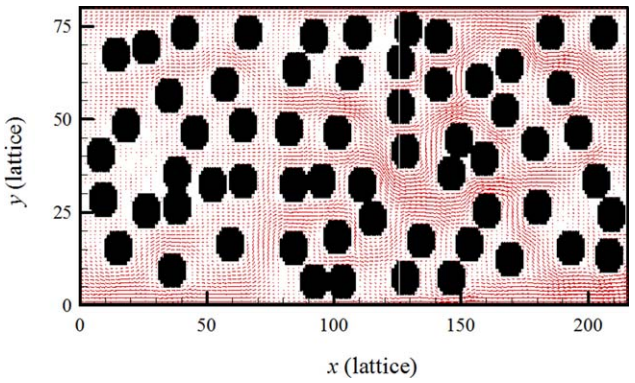

Figure 9. Macro velocity vectors inside the porous membrane MEM 5.

Transmembrane pressure difference $\Delta p = 0.05$. Pore structure, $\varepsilon_1 = 0.71$, $d_{p1} = 6.55\mu$m. [Color figure can be viewed in the online issue, which is available at wileyonlinelibrary.com.]

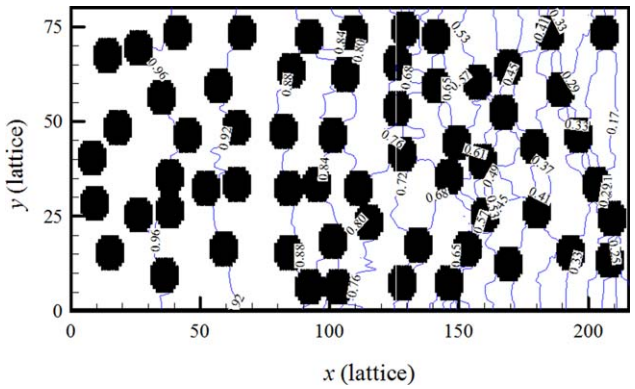

Figure 11. Concentration profiles inside the membrane with only the porous layer.

Transmembrane pressure difference $\Delta p = 0.05$. Pore structure, $\varepsilon_1 = 0.71$, $d_{p1} = 6.55\mu$m. [Color figure can be viewed in the online issue, which is available at wileyonlinelibrary.com.]

by the skin layer, only moisture can permeate through the composite membrane. There are no macro fluid flows inside the whole membrane. So in the modeling, macro velocity is set to zero, and density is set to 1.0, throughout the membrane lattices. Only mass transfer is simulated by LBM. The outlet boundary condition $C_{v,out} = 0.1$ is exerted on surface BC in Figure 3. Surface DE becomes an interface, where conjugate boundary conditions are exerted. The skin layer material is a modified PVA.[13] Physical properties are: partition coefficient $K_p = 25$, water diffusivity $D_{wm} = 3.6\times10^{-11}$ m^2/s, density $\rho_m = 800$ kg/m^3. Other operating conditions are similar to before.

The calculated mass flux vectors and concentration contours are plotted in Figure 12. In this figure, the porous support layer selected is MEM 6 in Table 1. The skin layer thickness is 2.5 μm. The mass fluxes are inhomogeneous in the support layer, but relatively uniform in the skin layer. The mass concentration and fluxes are continuous at the interface, meaning conjugate boundary conditions are satisfied. Since mass can only diffuse in the cavities of the first layer, the higher the porosity and pore diameters are, the better the composite membranes perform.

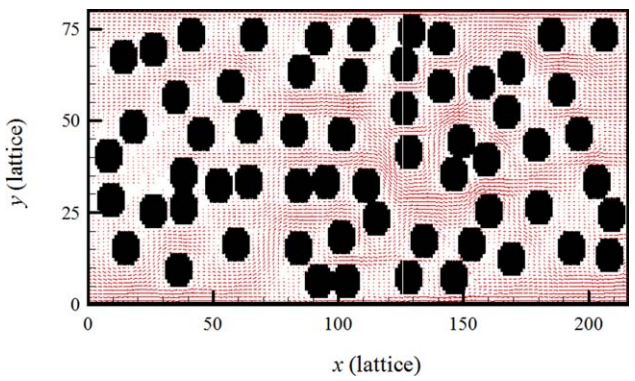

Figure 10. Mass flux vectors (*J*) inside the membrane with only the porous layer.

Transmembrane pressure difference $\Delta p = 0.05$. Pore structure, $\varepsilon_1 = 0.71$, $d_{p1} = 6.55$ μm. [Color figure can be viewed in the online issue, which is available at wileyonlinelibrary.com.]

Porous membranes generally have high porosity and large pore diameters, their permeability is high. The dominant resistance is in skin layer. Traditionally, decreasing the skin layer thickness is a key measure in optimizing performances of composite membranes. The effects can be seen in Figure 13, where the effects of skin layer thickness on composite membrane performances are depicted. A D_{wm} value of 1.41×10^{-12} m^2/s is used, which is for the traditional hygroscopic material before modifications.[5,13] The consequent equivalent vapor diffusivity in the second layer D_{e2}, the equivalent vapor diffusivity of the whole membrane D_e, and the skin layer to whole membrane resistance ratio ($\alpha_2 = r_2/r_{tot}$) are plotted for comparison. As seen, the equivalent vapor diffusivity in the skin layer does not change. Not surprisingly, the resistance ratio of layer two increases with its thickness. When the skin layer thickness is beyond 2 μm, it would account for 50% of the total resistance. Therefore, ultrathin skin layers should be prepared if the diffusivity of skin layer material is not high.

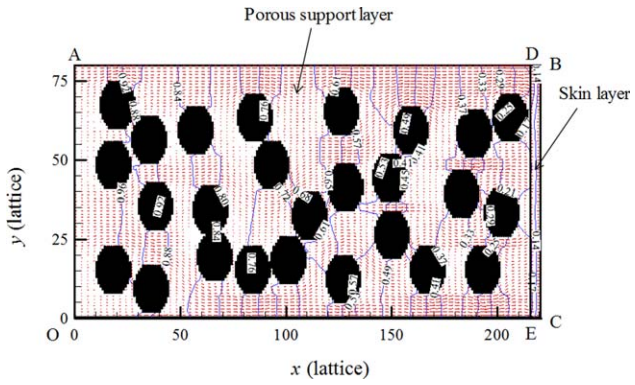

Figure 12. Mass flux vectors (*J*, the red vectors) and concentration contours (the blue lines) inside the composite membrane with a porous layer (OADE) and a skin layer (EDBC).

The first layer is MEM 6, $\delta_1 = 108.1$ μm, $\varepsilon_1 = 0.69$, $d_{p1} = 9.9$ μm. The second layer, $\delta_2 = 5\mu$m, $D_{wm} = 3.53\times10^{-11}$ m^2 s^{-1}. [Color figure can be viewed in the online issue, which is available at wileyonlinelibrary.com.]

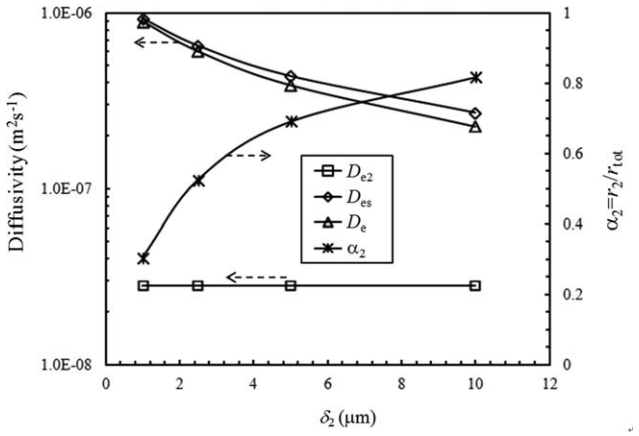

Figure 13. Effects of skin layer thickness on equivalent diffusivity and resistance ratio.

The first layer is MEM 2, $\delta_1 = 110.1$ μm, $\varepsilon_1 = 0.50$, $d_{p1} = 3.95$ μm. The second layer, $D_{wm} = 1.41 \times 10^{-12}$ m^2 s^{-1}.

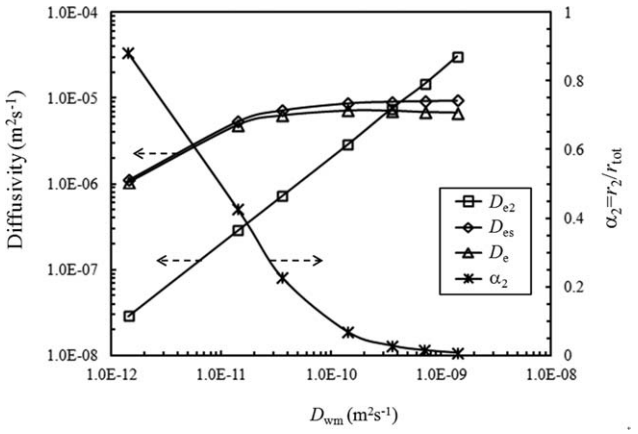

Figure 15. Effects of water diffusivity in the skin layer on equivalent diffusivity and resistance ratio.

The first layer is MEM 2, $\delta_1 = 110.1$ μm, $\varepsilon_1 = 0.50$, $d_{p1} = 3.95$ μm. The second layer, $\delta_2 = 5$ μm.

In previous analysis, black box models are used to clarify resistance. According to this method, the total resistance is expressed by

$$r_{tot} = r_1 + r_2 = \frac{\delta_1}{D_{e1}} + \frac{\delta_2}{D_{e2}} \tag{71}$$

where D_{e1} is the effective diffusivity of the porous layer. The overall effective diffusivity is calculated by

$$D_{es} = \frac{\delta_1 + \delta_2}{r_{tot}} \tag{72}$$

Subscript 's' here refers to 'series' because it is also called the series model. The calculated effective diffusivity by the series model is also plotted in above Figure 13. As seen, the series model deviates the LBM calculation to some extent. The larger the skin layer thickness is, the larger the deviation is.

Another alternative to enhance mass transfer is to modify skin layer materials to have an increased diffusivity. This can be done by either increasing D_{wm} or increasing K_p (the solubility).

Figure 14 shows the effects of water diffusivity in the skin layer on the performances. Figure 15 shows a similar graph, but with a different porous support layer. From these two figures, it is seen that the higher the water diffusivity in the skin layer is, the less the resistance ratio of the first layer is. The ratio decreases quickly when D_{wm} is from 10^{-12} to 10^{-10} m^2/s. With the modified PVA skin layer[13] with a D_{wm} value of 3.6×10^{-11} m^2/s, it accounts for less than 30% of the total resistance. To increase the diffusivity or solubility of the skin layer is a more effective way to augment mass transfer.

When the skin layer is improved, the porous support layer also plays dominant roles. As seen from above two figures, with the modified material and a more porous support layer of MEM 6, the resistance ratio is around 0.3. When a less porous support layer of MEM 2 is used, the ratio is about 0.18. It indicates that the dominant resistance now is in porous layer side. So besides selecting skin layers of high permeability, more porous support layers should be used.

The skin layer, though very thin, plays a leading role in the overall performances of the composite membranes.

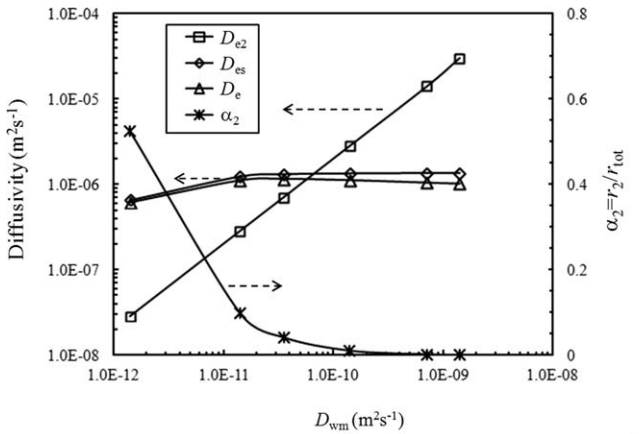

Figure 14. Effects of water diffusivity in the skin layer on equivalent diffusivity and resistance ratio.

The first layer is MEM 6, $\delta_1 = 108.1$ μm, $\varepsilon_1 = 0.69$, $d_{p1} = 9.9$ μm. The second layer, $\delta_2 = 5$ μm.

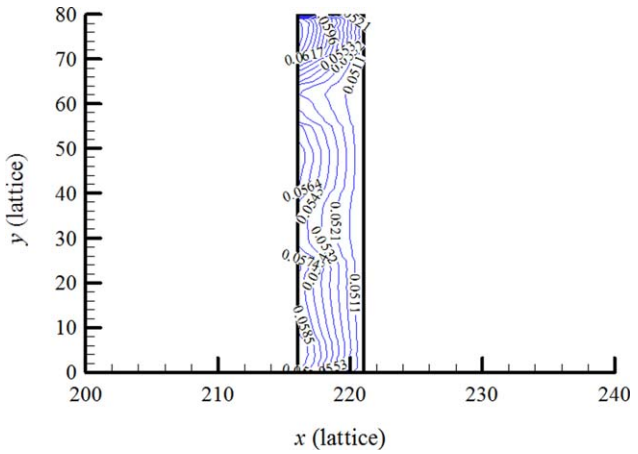

Figure 16. Contours of water uptake (kg water/kg membrane) in the skin layer.

$D_{e2}/D_v = 0.5$. [Color figure can be viewed in the online issue, which is available at wileyonlinelibrary.com.]

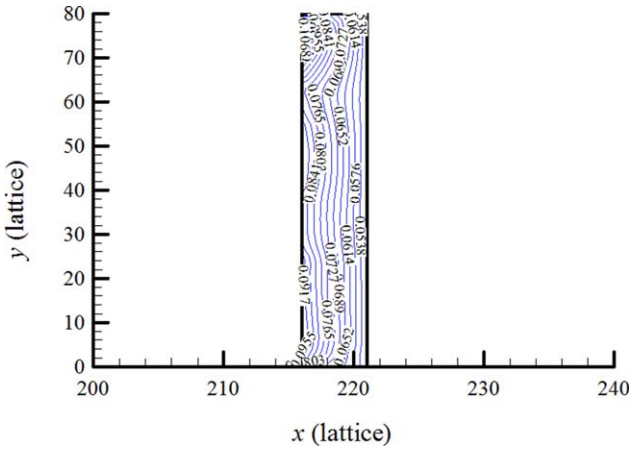

Figure 17. Contours of water uptake (kg water/kg membrane) in the skin layer.

$D_{e2}/D_v = 0.01$. [Color figure can be viewed in the online issue, which is available at wileyonlinelibrary.com.]

Previous macroscopic CFD software can hardly be used to evaluate the transport details in this layer. Now with this mesoscale methodology, the effects can be studied.

To see the transport phenomena in the skin layer more clearly, concentration contours in the second layer have been plotted in Figure 12. However, they are not the "real" concentration contours in this dense material. They are the "hypothetic" moisture concentrations which are in equilibrium with the real water uptake in the material. To see the real distribution of water uptake, calculated equilibrium moisture concentrations are converted to water uptake by the partition coefficient. The contours are seen in Figures 16 and 17 for two skin layer materials, one with a high equivalent diffusivity ($D_{e2}/D_v = 0.5$) and another with a low equivalent diffusivity ($D_{e2}/D_v = 0.01$, which is common in traditional water-permeable materials[5,13,32]).

From these two figures, it is seen that the distributions of water in the skin layer are in fact inhomogeneous as well. The higher the diffusivity is, the more serious the inhomogeneity is, which would compromise the whole membrane effective diffusivity. This nonuniformity is resulted from the nonuniform distributions of moisture concentrations in the first layer. The inhomogeneity in the skin layer also explains the reason why the series model overpredicts membrane performance.

Above analysis discloses that mass transfer in the composite membrane is a close interaction between the porous support layer and the skin layer. For the traditional materials with relatively low diffusivity, dominant resistance is in the skin layer. Though to decrease the skin layer thickness is effective, to modify the materials is more influential to augment mass transfer. For the modified materials, either by diffusivity or by solubility, dominant resistance would return to the porous part. Two layers should be optimized together. This LBM study provides some new guidelines for future performance optimization of composite membranes.

Conclusions

Composite membranes are the most important class of membranes for gas separations. The mesoscale nature of the transport phenomena in the membrane, and the complexity in membrane structures, make the modeling of mass transfer inside the structure a difficult task. The traditional black box modeling approach gives no detailed information inside. This study uses a new approach, LBM simulations approach. The whole membrane is separated into two parts with distinct different structures. Fluid flow and mass profiles are calculated to estimate the overall performance. The results can be found:

1. The proposed methodology can model pore-scale fluid flow and mass transfer satisfactorily. Appropriate boundary conditions are proposed, especially for membranes with layers of different transport mechanisms. They are connected by an interface with mass and flux continuity.

2. For solely the porous membrane under transmembrane pressure difference, the dominant mechanism is combined Poiseuille flow and ordinary diffusion. The permeability is high due to macro fluid flow. With such support layers, the dominant resistance is in the skin layer with unmodified materials. Increasing the equivalent diffusivity of the skin layer, by diffusivity or by solubility, is more effective than decreasing its thickness to augment mass transfer. Design guidelines should be changed from optimizing skin layer thickness to modifying compositions of the skin layer.

3. The LBM simulations disclose the nonuniform distributions of mass transfer inside the composite membrane both in the porous layer and the skin layer. Traditional black box series model over predicts the membrane performance, especially with skin materials of high diffusivity, because the mesoscale inhomogeneity cannot be disclosed with the traditional macroscale approach.

Acknowledgment

This Project 51376064 is supported by National Natural Science Foundation of China.

Notation

C = mass concentration/uptake, kg vapor/kg dry air
c = speed, m/s
c_p = specific heat, $kJkg^{-1}\ K^{-1}$
d_p = pore diameter, m
D = diffusivity, m^2/s
$\boldsymbol{e}$ = vector
f = distribution function for density
g = distribution function for concentration
h = convective heat-transfer coefficient, $kWm^{-2}\ K^{-1}$
I_s = index function for porous media
J = mass flux, $kgm^{-2}\ s^{-1}$
k = convective mass-transfer coefficient, ms^{-1}
K = partition coefficient, kg water/kg material/kg moisture/kg dry air
L = length, m
Ma = Mach number
N = number of pixels
Nu = Nusselt number
p = pressure, Pa
Pe = permeability, m^2
Pr = Prandtl number
r_1 = specific heat ratio
r = resistance, sm^{-1}
Re = Reynolds number
S = function for porous media
Sc = Schmidt number
Sh = Sherwood number
T = temperature, K
t = time, s
u = velocity, ms^{-1}
U = velocity difference, ms^{-1}
W = weight coefficient
x = coordinate, m
y = coordinate, m

Greek letters

ρ = density, kgm^{-3}
ε = porosity
δ = thickness, μm
α = weight
λ = ratio
τ = relaxation time
ν = kinematic viscosity, m^2s^{-1}
λ_v = mean free path of vapor, m
θ = angle, rad

Superscripts

′ = variables with physical units
eq = equilibrium
p = porous layer
s = skin layer

Subscripts

0 = characteristic variables
c = cell
e = effective
h = heat
in = inlet
K = Knudsen
m = mass, mean, membrane
O = ordinary
out = outlet
P = Poiseuille
s = solid, sound
tot = total
v = vapor, viscosity
w = wall, water
α = direction, x or y

Literature Cited

1. Pan FS, Jia HP, Cheng QL, Jiang ZY. Bio-inspired fabrication of composite membranes with ultrathin polymer-silica nanohybrid skin layer. *J Membr Sci*. 2010;362:119–126.
2. Liu L, Chen Y, Li SG, Deng MC. The effect of a support layer on the permeability of water vapor in asymmetric composite membranes. *Sep Sci Technol*. 2001;36:3701–3720.
3. Yuan F, Wang Z, Li SC, Wang JX, Wang SC. Formation-structure-performance correlation of thin film composite membranes prepared by interfacial polymerization for gas separation. *J Membr Sci*. 2012; 421–422:327–341.
4. Huang SM, Zhang LZ. Researches and trends in membrane-based liquid desiccant air dehumidification. *Renewable Sustainable Energy Rev*. 2013;28:425–440.
5. Zhang LZ. Progress on heat and moisture recovery with membranes: from fundamentals to engineering applications. *Energy Conversion Manage*. 2012;63:173–195.
6. Kistler KR, Cussler EL. Membrane modules for building ventilation. *Chem Eng Res Des*. 2002;80:53–64.
7. Markovic A, Stoltenberg D, Enke D, Schlunder EU, Seidel-Morgenstern A. Gas permeation through porous glass membranes, Part I. Mesoporous glasses-effect of pore diameter and surface properties. *J Membr Sci*. 2009;336:17–31.
8. Suwanwarangkul R, Croiset E, Fowler MW, Douglas PL, Entchev E, Douglas MA. Performance comparison of Fick's, dusty-gas and Stefan–Maxwell models to predict the concentration overpotential of a SOFC anode. *J Power Sources*. 2003;122:9–18.
9. Gruber MF, Johnson CJ, Tang CY, Jensen MH, Yde L, Helix-Nielsen C. Computational fluid dynamics simulations of flow and concentration polarization in forward osmosis membrane systems. *J Membr Sci*. 2011;379:488–495.
10. Fang YM, Duranceau SJ. Comparison of nonhomogeneous and homogeneous mass transfer in reverse osmosis membrane processes. *Desalination Water Treat*. 2013;51:6444–6458.
11. Prasad R, Sirkar KK. Solvent extraction with microporous hydrophilic and composite membranes. *AIChE J*. 1987;33:1057–1066.
12. Thomas S, Schafer R, Caro J, Seidel-Morgenstern A. Investigation of mass transfer through inorganic membranes with several layers. *Catal Today*. 2001;67:205–216.
13. Zhang LZ, Wang YY, Wang CL, Xiang H. Synthesis and characterization of a PVA/LiCl blend membrane for air dehumidification. *J Membr Sci*. 2008;308:198–206.
14. Dixon AG, Nijemeisland M. CFD as a design tool for fixed-bed reactors. *Ind Eng Chem Res*. 2001;40:5246–5254.
15. Joshi JB, Ranade VV. Computational fluid dynamics for designing process equipment: expectations, current status, and path forward. *Ind Eng Chem Res*. 2003;42:1115–1128.
16. Tan KK, Tan YW, Choong TSY. Onset of natural convection induced by bottom-up transient mass diffusion in porous media. *Powder Technol*. 2009;191:55–60.
17. Coasne B, Galarneau A, Gerardin C, Fajula F, Villemot F. Molecular simulation of adsorption and transport in hierarchical porous materials. *Langmuir*. 2013;29:7864–7875.
18. Wang LY, Dumont RS, Dickson JM. Nonequilibrium molecular dynamics simulation of pressure-driven water transport through modified CNT membranes. *J Chem Phys*. 2013;138:124701–124709.
19. Yoshino M, Inamuro T. Lattice Boltzmann simulations for flow and heat/mass transfer problems in a three-dimensional porous structure. *Int J Numer Methods Fluids*. 2003;43:183–198.
20. Chen L, Feng YL, Song CX, Chen L, He YL, Tao WQ. Multi-scale modeling of proton exchange membrane fuel cell by coupling finite volume method and lattice Boltzmann method. *Int J Heat Mass Transfer*. 2013;63:268–283.
21. Chen L, Luan HB, He YL, Tao WQ. Pore-scale flow and mass transport in gas diffusion layer of proton exchange membrane fuel cell with interdigitated flow fields. *Int J Therm Sci*. 2012;51:132–144.
22. Kim SH, Pitsch H. Reconstruction and effective transport properties of the catalyst layer in PEM fuel cells. *J Electrochem Soc*. 2009; 156:B673–B681.
23. Yablecki J, Nabovati A, Bazylak A. Modeling the effective thermal conductivity of an anisotropic gas diffusion layer in a polymer electrolyte membrane fuel cell. *J Electrochem Soc*. 2012;159:B647–B653.
24. Zhang LZ. An analytical solution for heat mass transfer in a hollow fiber membrane based air-to-air heat mass exchanger. *J Membr Sci*. 2010;360:217–225.
25. Yeong CLY, Torquato S. Reconstructing random media. *Phys Rev E*. 1998;57:495–505.
26. Humby SJ, Biggs MJ, Tuzun U. Explicit numerical simulation of fluids in reconstructed porous media. *Chem Eng Sci*. 2002;57:1955–1968.
27. Sullivan SP, Sani FM, Johns ML, Gladden LF. Simulation of packed bed reactors using lattice Boltzmann methods. *Chem Eng Sci*. 2005; 60:3405–3418.
28. Verma N, Mewes D. Lattice Boltzmann methods for simulation of micro and macrotransport in a packed bed of porous adsorbents under non-isothermal condition. *Comput Math Appl*. 2009;58:1003–1014.
29. Imamura T, Suzuki K, Nakamura T, Yoshida M. Acceleration of steady-state lattice Boltzmann simulations on non-uniform mesh using local time step method. *J Comput Phys*. 2005;202:645–663.
30. Zou Q, He Y. On pressure and velocity boundary conditions for the lattice Boltzmann BGK model. *Physics of Fluids*. 1997;9:1591–1598.
31. Cussler EL. *Diffusion-Mass Transfer in Fluid systems*. Cambridge: Cambridge University Press, 2000.
32. Zhang LZ. Evaluation of moisture diffusivity in hydrophilic polymer membranes: a new approach. *J Membr Sci*. 2006;269:75–83.
33. Maier RS, Bernard RS, Grunau DW. Boundary conditions for the lattice Boltzmann method. *Phys Fluids*. 1996;8:1788–1800.
34. Zhang LZ. *Conjugate Heat and Mass Transfer in Heat Mass Exchanger Ducts*, 1st Edition. New York: Academic Press, Elsevier, 2013.
35. Incropera FP, Dewitt DP. *Introduction to Heat Transfer*, 3rd ed. New York: Wiley, 1996.

Appendix A: Deduction of First-Order Nonequilibrium Part of Distribution Function

Here, we develop an algorithm to transfer the macro concentrations into concentration distribution functions with a scheme similar to[29]

$$g_i = g_i^{eq} + g_i^{(1)} \tag{A1}$$

The Chapman–Enskog expansion is applied to the lattice Boltzmann equation, the first order of nonequilibrium is described by

$$g_i^{(1)} = -\tau_m \Delta t \cdot \left(\frac{\partial g_i^{eq}}{\partial t} + e_{ix} \frac{\partial g_i^{eq}}{\partial x} + e_{iy} \frac{\partial g_i^{eq}}{\partial y} \right) \tag{A2}$$

The time and special derivatives of the equilibrium distribution function of Eq. A2 are replaced by the derivatives of the macroscopic variables as

$$\frac{\partial g_i^{\mathrm{eq}}}{\partial t}=\frac{\partial g_i^{\mathrm{eq}}}{\partial(\rho \mathrm{C_v})}\frac{\partial(\rho \mathrm{C_v})}{\partial t}+\frac{\partial g_i^{\mathrm{eq}}}{\partial u_x}\frac{\partial u_x}{\partial t}+\frac{\partial g_i^{\mathrm{eq}}}{\partial u_y}\frac{\partial u_y}{\partial t} \tag{A3}$$

$$\frac{\partial g_i^{\mathrm{eq}}}{\partial x}=\frac{\partial g_i^{\mathrm{eq}}}{\partial(\rho \mathrm{C_v})}\frac{\partial(\rho \mathrm{C_v})}{\partial x}+\frac{\partial g_i^{\mathrm{eq}}}{\partial u_y}\frac{\partial u_y}{\partial x}+\frac{\partial g_i^{\mathrm{eq}}}{\partial u_x}\frac{\partial u_x}{\partial x} \tag{A4}$$

$$\frac{\partial g_i^{\mathrm{eq}}}{\partial y}=\frac{\partial g_i^{\mathrm{eq}}}{\partial(\rho \mathrm{C_v})}\frac{\partial(\rho \mathrm{C_v})}{\partial y}+\frac{\partial g_i^{\mathrm{eq}}}{\partial u_x}\frac{\partial u_x}{\partial y}+\frac{\partial g_i^{\mathrm{eq}}}{\partial u_y}\frac{\partial u_y}{\partial y} \tag{A5}$$

The equilibrium distribution functions differentiated by the macroscopic variables, from Eq. 12, are

$$\frac{\partial g_i^{\mathrm{eq}}}{\partial(\rho \mathrm{C_v})}=\frac{1}{\rho \mathrm{C_v}}g_i^{\mathrm{eq}} \tag{A6}$$

$$\frac{\partial g_i^{\mathrm{eq}}}{\partial u_x}=W_i\rho C_{\mathrm{v}}\left(\frac{1}{c_{\mathrm{s}}^2}e_{ix}\right) \tag{A7}$$

$$\frac{\partial g_i^{\mathrm{eq}}}{\partial u_y}=W_i\rho C_{\mathrm{v}}\left(\frac{1}{c_{\mathrm{s}}^2}e_{iy}\right) \tag{A8}$$

where e_{ix} is the shadow of $\boldsymbol{e}_{\mathrm{i}}$ on x axis. The first-order derivatives of mass fraction continuity and the momentum continuity (macroscopic N-S equations) are

$$\frac{\partial(\rho C_v)}{\partial t}=-\frac{\partial(\rho C_v)u_{\mathrm{x}}}{\partial x}-\frac{\partial(\rho C_v)u_{\mathrm{y}}}{\partial y} \tag{A9}$$

$$\frac{\partial u_{\mathrm{x}}}{\partial t}=-u_{\mathrm{x}}\frac{\partial u_{\mathrm{x}}}{\partial x}-u_{\mathrm{x}}\frac{\partial u_{\mathrm{y}}}{\partial y}-\frac{1}{\rho}\frac{\partial p}{\partial x} \tag{A10}$$

$$\frac{\partial u_{\mathrm{y}}}{\partial t}=-u_{\mathrm{y}}\frac{\partial u_{\mathrm{x}}}{\partial x}-u_{\mathrm{y}}\frac{\partial u_{\mathrm{y}}}{\partial y}-\frac{1}{\rho}\frac{\partial p}{\partial y} \tag{A11}$$

Substituting Eqs.A3–A11 into A2, the first order of nonequilibrium is given from the macroscopic variables as

$$\begin{aligned}g_i^{(1)}=&-\tau_{\mathrm{m}}\Delta t\cdot\left[U_{\mathrm{ix}}\frac{g_i^{\mathrm{eq}}}{\rho C_{\mathrm{v}}}\frac{\partial(\rho C_{\mathrm{v}})}{\partial x}+U_{iy}\frac{g_i^{\mathrm{eq}}}{\rho C_{\mathrm{v}}}\frac{\partial(\rho C_{\mathrm{v}})}{\partial y}\right.\\&+\frac{W_i\rho C_{\mathrm{v}}U_{ix}e_{iy}}{c_{\mathrm{s}}^2}\frac{\partial u_y}{\partial x}+\frac{W_i\rho C_{\mathrm{v}}U_{iy}e_{ix}}{c_{\mathrm{s}}^2}\frac{\partial u_x}{\partial y}-g_i^{\mathrm{eq}}\frac{\partial u_x}{\partial x}\\&\left.-g_i^{\mathrm{eq}}\frac{\partial u_y}{\partial y}-W_iC_{\mathrm{v}}e_{ix}\frac{\partial \rho}{\partial x}-W_iC_{\mathrm{v}}e_{iy}\frac{\partial \rho}{\partial y}\right]\end{aligned} \tag{A12}$$

where

$$U_{i\alpha}=e_{\mathrm{i}\alpha}-u_\alpha \tag{A13}$$

and here $\alpha=x,\ y$. Then at last, the distribution functions at the inlet and outlet are calculated by Eq. A1.

Manuscript received Jan. 25, 2014, and revision received June 16, 2014.